Structural polymorphism of amyloid fibrils in cardiac ATTR amyloidosis revealed by cryo-electron microscopy

Nguyen, Binh A.[1], Afrin, Shumaila[1], Singh, Virender[1], Ahmed, Yasmin[1], Pedretti, Rose [1], Fernandez-Ramirez, Maria Del Carmen[1], Benson, Merrill D.[2], Sawaya R. Michael[3], Cao, Qin[3,4], Boyer, David[3], Pope, Alexander[5], Wydorski, Pawel M.[1], Chhapra, Farzeen[1], Eisenberg, David S.[3], Saelices, Lorena[1]

[1]*Center for Alzheimer's and Neurodegenerative Diseases, Department of Biophysics, University of Texas Southwestern Medical Center (UTSW), Dallas, TX, USA*

[2]*Department of Pathology and Laboratory Medicine, Indiana University School of Medicine, Indianapolis, IN, USA*

[3]*Department of Biological Chemistry, University of California, Los Angeles, Howard Hughes Medical Institute, CA, USA*

[4]*Current address: Key Laboratory for the Genetics of Developmental and Neuropsychiatric Disorders (Ministry of Education), Bio-X Institutes, Shanghai Jiao Tong University, Shanghai, China*

[5]*Department of Neuroscience, University of Texas Southwestern Medical Center, Dallas, TX, USA*

Keywords: Cryo-EM, amyloid, transthyretin, ATTR

Abstract

ATTR amyloidosis is a fatal disease associated with the accumulation of transthyretin (ATTR) fibrils that lead to organ failure and death. Mutations in the *TTR* gene or aging may accelerate the deposition of variant (ATTRv) or wild-type (ATTRwt) transthyretin, respectively. Although ATTR amyloidosis patients accumulate ATTR fibrils in virtually every organ, the clinical presentation is often unpredictable and variable. Recent studies in cryo-electron microscopy (cryo-EM) have revealed that in tauopathies and synucleinopathies, diseases involving amyloidosis of tau and α-synuclein, respectively, all the patients of the same disease display the same fibril fold, or *polymorph*. In this study, we use cryo-EM to explore whether fibrils from heart tissue of different patients with cardiac ATTR amyloidosis share a common fold. We determined the molecular structures of fibrils extracted from the hearts of seven patients, including both ATTRv and ATTRwt carriers, at resolutions of 3.0 to 3.7 Å. We found that ATTRv mutations perturb the fibril conformation whereas ATTRwt fibrils share a common structure fold. Our findings suggest that unlike in tauopathies and synucleinopathies, ATTRv fibrils display structural polymorphism driven by each individual and their genotypes. ATTR polymorphism challenges the current paradigm of "one disease equals one fibril polymorph," and questions whether similarly novel conformations occur in other amyloidoses.

Introduction

Amyloidoses are a group of fatal disorders caused by the pathological accumulation of amyloid fibrils in affected organs[1]. They have in common that they are phenotypically variable and often diagnosed too late for treatments

and interventions to be effective. Amyloid fibrils strongly resist degradation and clearance because they are composed of proteins that self-assemble into highly ordered and stable β-sheet-rich structures[2].

In ATTR amyloidosis, the amyloid fibrils are composed of the amyloidogenic form of the hormone transporter transthyretin (ATTR)[3]. ATTR self-assemblage caused by mutations in the *TTR* gene leads to variant ATTR (ATTRv) amyloidosis. Other unknown processes related to age lead to wild-type ATTR (ATTRwt) amyloidosis. The clinical presentation of ATTRv amyloidosis is unpredictable and variable, often manifesting between 25 and 65 years of age with polyneuropathy, autonomic neuropathy, gastrointestinal and eye involvement, carpal tunnel syndrome, spinal canal stenosis, and/or cardiomyopathy[4]. The clinical presentation of ATTRwt is more predictable and better characterized; it manifests later in life (>60 years old) as cardiomyopathy, and mainly affects men[5]. The roots of the phenotypic variability of ATTR amyloidosis are yet unknown: is it connected to heterogeneity of fibril structures, or to characteristics of the surrounding tissue, or to other factors?

Recent cryo-electron microscopy (cryo-EM) studies on tauopathies and synucleinopathies, a set of brain amyloid diseases respectively associated with the deposition of tau and α-synuclein, have looked for the source of their poorly understood phenotypic variability[6–9]. These studies reveal that fibrils from patients presenting the same disease share the same fold, or *polymorph*, supporting the idea that the fibril structure determines disease presentation[10]. But studies focused on brain diseases offer limited information about whether amyloid formation is influenced by the type of tissue or the mutation.

There are two studies that associate ATTR amyloidosis with the formation of distinct fibril polymorphs in two different organs: the heart[11] and the vitreous humor[12]. Both cases involved the same pathological mutation, ATTRV30M; however, the small number of patients limits the studies' strength and does not rule out whether mutations or tissue type could affect amyloid structure.

In this study, we focus on the structure of cardiac ATTR fibrils to evaluate structural polymorphism in the heart. We used cryo-EM to determine the molecular structure of fibrils extracted from seven patients with ATTR amyloidosis—two ATTRwt cases and five ATTRv. We found that ATTR mutations perturb the fibril fold locally at the mutation site, suggesting that the degree of structural polymorphism in ATTR fibrils may be driven by the individual and their genotype. These results show that, contrary to tauopathies, ATTR amyloidosis patients can present structural variation in their fibrils, even when carrying the same variant. Additional studies on organ-specific structural heterogeneity and the influence of fibril folding in clinical presentations are warranted. A deeper structural understanding of ATTR amyloid fibrils could aid development of new therapeutic and diagnostic strategies to improve patients' prognosis and quality of life.

Results

ATTR fibrils extraction from frozen and lyophilized samples.

We obtained freshly frozen cardiac tissue from a total of seven patients, two carried wild types (ATTRwt) and five hereditary variants (ATTRv) (ATTRP24S, ATTRT60A, two ATTRI84S, and ATTRV122I). Supplementary Table 1 lists the details of each sample. We used the purification method described by Schmidt et al. to extract ATTR fibrils from frozen cardiac tissue (Supplementary Figure 1A)[11]. This method starts with washing of minced tissue with a tris-calcium buffer, followed by the resuspension of the pellet and its incubation with collagenase overnight. Finally, we incubated the samples with EDTA and used ice water to extract amyloid into the soluble fraction. Pure ATTR fibrils from frozen cardiac tissues eluted after one or two rounds of washing and centrifugation with ice water. We confirmed the purity of ATTR fibril extracts and their suitability for cryo-EM structure determination using transmission electron microscopy with negative staining (Supplementary Figure 1B). We also established the fibrillar content of the extracts by analyzing their capacity to seed TTR aggregation

in vitro (Supplementary Figure 1C). Finally, we screened and optimized samples for cryo-EM imaging (Supplementary Figure 2).

ATTRwt fibrils extracted from two different patients share a common core.

We collected cryo-EM images of the fibrils extracted from the hearts of two ATTRwt amyloidosis patients, ATTRwt-1 and ATTRwt-2. Two-dimensional (2D) classification discerned two polymorphs that differ in their twisting (Figure 1A and Supplementary Figure 3). The most prevalent species presented a clear twist, here referred to as *curvy* fibrils, and accounted for at least 95% of the extracted particles (Supplementary Table 2). The *straight* species was not suitable for structure determination because it lacked a twist (Figure 1A).

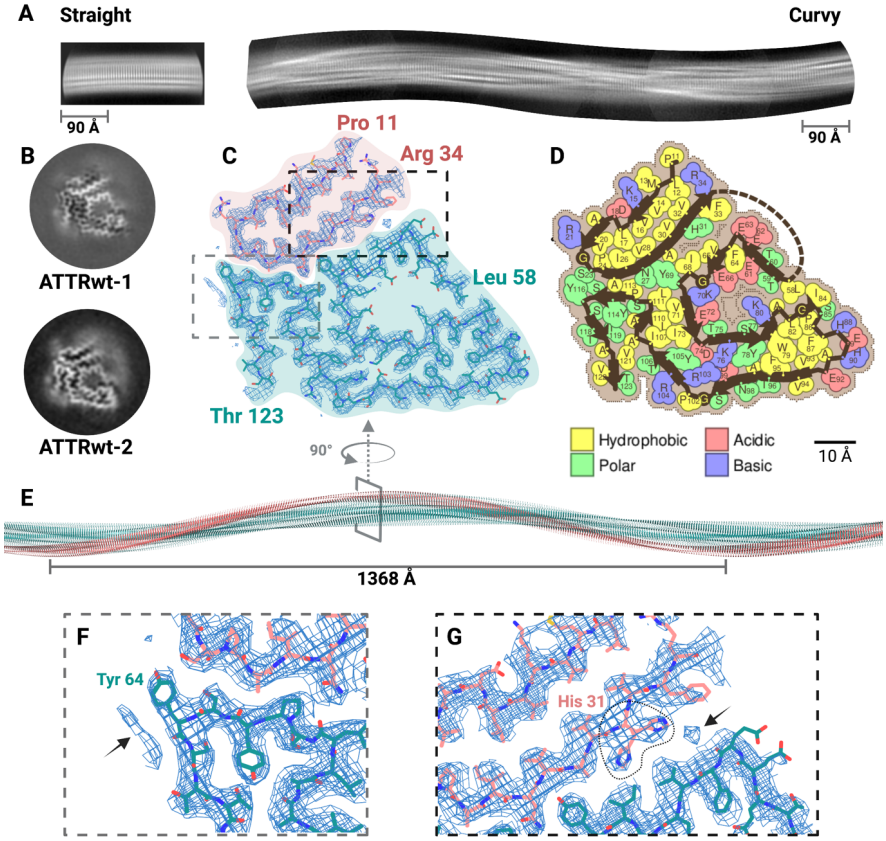

Figure 1. Cryo-EM structure of cardiac fibrils from an ATTRwt amyloidosis patient. A. Representative 2D class averages of straight fibrils (left) and curvy fibrils after stitching (right). **B.** Three-dimensional (3D) class averages of curvy fibrils from ATTRwt-1 and WTTRwt-2 patients. **C.** Cryo-EM density and atomic model of ATTRwt-1 fibrils. The model contains two fragments of transthyretin colored pink (residues Pro 11 to Arg 34) and turquoise (residues Leu 58 to Thr 123). **D.** Schematic view of the fibril core showing residue composition in patient ATTRwt-1. **E.** Model reconstruction of an ATTRwt-1 fibril. **F.** Close view of an unsatisfied density neighboring the residue Tyr 64 in ATTRwt-1 fibrils marked with an arrow. **G.** Close view of the interface between the N and C terminal fragments, pointing to unsatisfied densities in ATTRwt-1 fibrils. One density blob could be assigned to an alternative rotamer of His 31 (dashed line).

Using helical reconstruction, we determined the cryo-EM structures of curvy ATTR fibrils extracted from the two patients. The overall resolution of the ATTRwt-1 and ATTRwt-2 structures were 3.3 and 3.7 Å, respectively. Both structure cores shared the same fold (Figure 1B), with one single protofilament composed of two ATTR fragments: Pro 11 to Lys 35 and Gly 57 to Thr 123 (Figure 1C and Supplementary Figure 1C). The overall secondary structure of each chain is summarized in Supplementary Figure 4, and contains highly interdigitated interfaces mostly made of hydrophobic residues, also known as *steric zippers*[13], and a polar channel that involves residues from Gly 58 to Ile 84 (Figure 1D). ATTRwt-1 fibrils presented a crossover length of 684 Å with a helical twist of –1.25º and a helical rise of 4.75 Å (Figure 1E). ATTRwt-2 fibrils presented a crossover length of 663 Å with a helical twist of –1.29º and a helical rise of 4.78 Å (Supplementary Table 2 and Supplementary Figure 3).

Curvy ATTRv fibrils come in different flavors.

Using the same method as for ATTRwt fibrils, we extracted fibrils from five ATTRv amyloidosis patients, carrying the variants ATTRP24S, ATTRT60A, ATTRI84S, and ATTRV122I (Supplementary Table 1). As with ATTRwt fibrils, all the samples yielded the curvy and the straight fibrils seen in ATTRwt fibrils during 2D classification (Supplementary Table 2). Although the proportion of curvy and straight fibrils differed for the patients, the curvy folding predominated in all cases (Supplementary Table 2).

The helical reconstruction of curvy fibrils from variants ATTRP24S and ATTRT60A yielded structures resembling those of ATTRwt fibrils in crossover distance, helical twist, helical rise, and overall structural fold (Figure 2 and Supplementary Table 2). However, curvy ATTRV122I fibrils extracted from one patient yielded two distinct curvy populations with different crossover distances and helical twists (Figure 3 and Supplementary Table 2). These two populations share a similar structure fold, and identical helical rise (Figure 5C-F and Supplementary Table 2). The subtle difference in the fold of these two populations is that ATTRV122Ib fibrils contain 4 additional residues at the beginning of the the C-terminal segment (Figure 3E) and 4 additional residues at the end of the C-terminal segment (Figure 3F). The residue compositions of these fibrils are shown in Supplementary Figure 5.

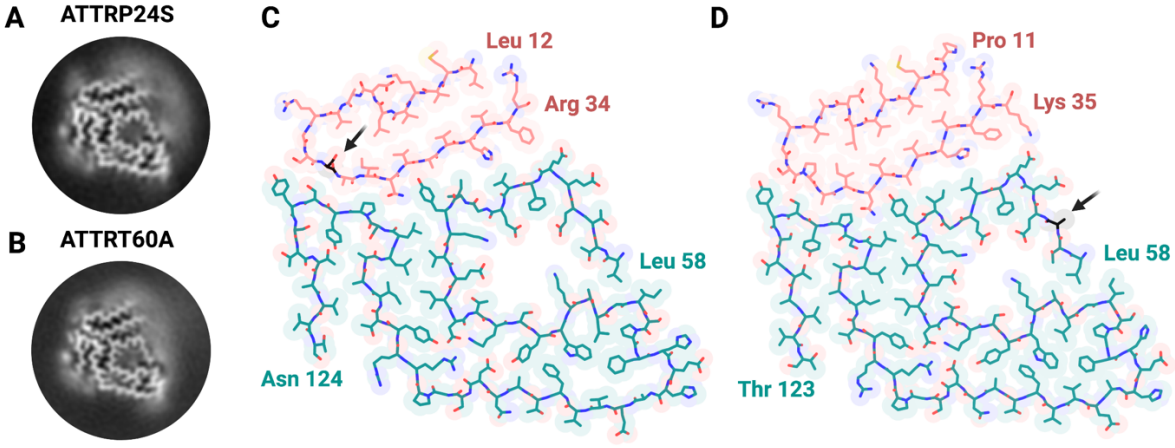

Figure 2. Cryo-EM structures of cardiac fibrils from ATTRP24S and ATTRT60A amyloidosis patients. A and B. 3D class averages of curvy fibrils from ATTRP24S (**A**) and ATTRT60A (**B**) patients. **C and D.** Cryo-EM density and atomic model of ATTRP24S (**C**) and ATTRT60A (**D**) fibrils. The model contains two fragments of transthyretin. The N terminal segment is colored pink, encompassing residues Leu 12 to Arg 34 (**C**) and Pro 11

to Lys 35 (**D**). The C terminal segment is colored turquoise, encompassing residues Leu 58 to Asn 124 (**C**) and Leu 58 to Thr 123 (**D**). Arrows point at the mutation site.

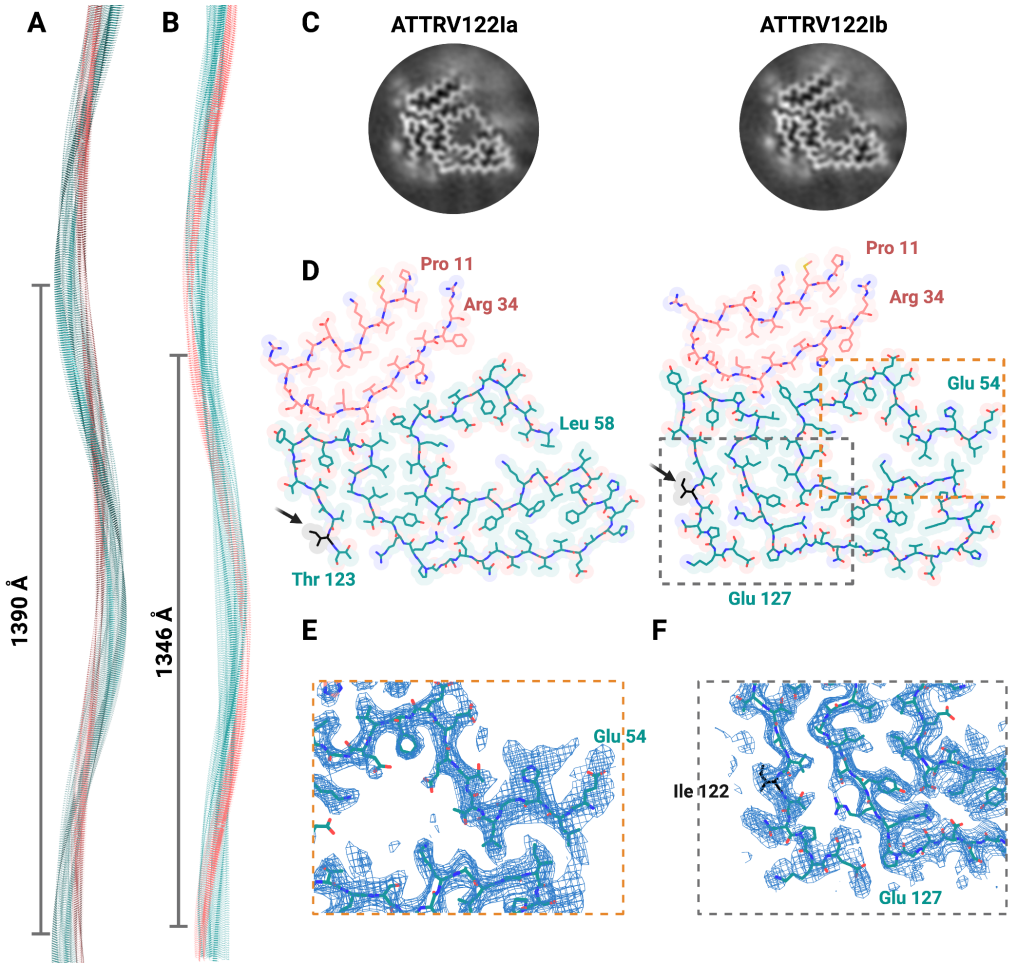

Figure 3. Cryo-EM structures of two distinct ATTRV122I fibrils extracted from the same patient. A and B. Model reconstructions of two distinct ATTRV122I fibrils from the same patient. They differ in the helical twist angle and crossover distance. **C.** 3D class averages of the two types of fibrils. **D.** Atomic model of ATTRV122I fibrils (Left, ATTRV122Ia; Right, ATTRV122Ib). The two fragments of transthyretin are colored pink (N terminus) and turquoise (C terminus). Arrows point at the mutation site. **E and F.** Enlarged view of the cryo-EM density and atomic model of the additional residues found in ATTRV122Ib fibrils: residues Glu 54 onwards (**E**) and Glu 127 backwards (**F**).

Cardiac ATTR fibrils extracted from an ATTRI84S patient, ATTRI84S-1 (Supplementary Table 1), yielded curvy fibrils resembling ATTRwt fibrils (Figure 4A and Supplementary Table 2). However, there was a significant difference—the segment prior to Gly 67 of the C-terminal fragment of ATTRI84S-1 fibrils appeared disordered or absent (Figure 4B-D). Intrigued by this finding, we set out to determine the structure of fibrils extracted from an additional ATTRI84S patient, ATTRI84S-2 (Figure 4E-H). These fibrils share crossover distances and helical twists with ATTRI84S-1 fibrils (Figure 4E and Supplementary Table 3). However, they have a defined density for residues Thy 59 to Gly 67 (Figure 4F-H), one residue short to fibrils from ATTRwt or the other ATTRv patients.

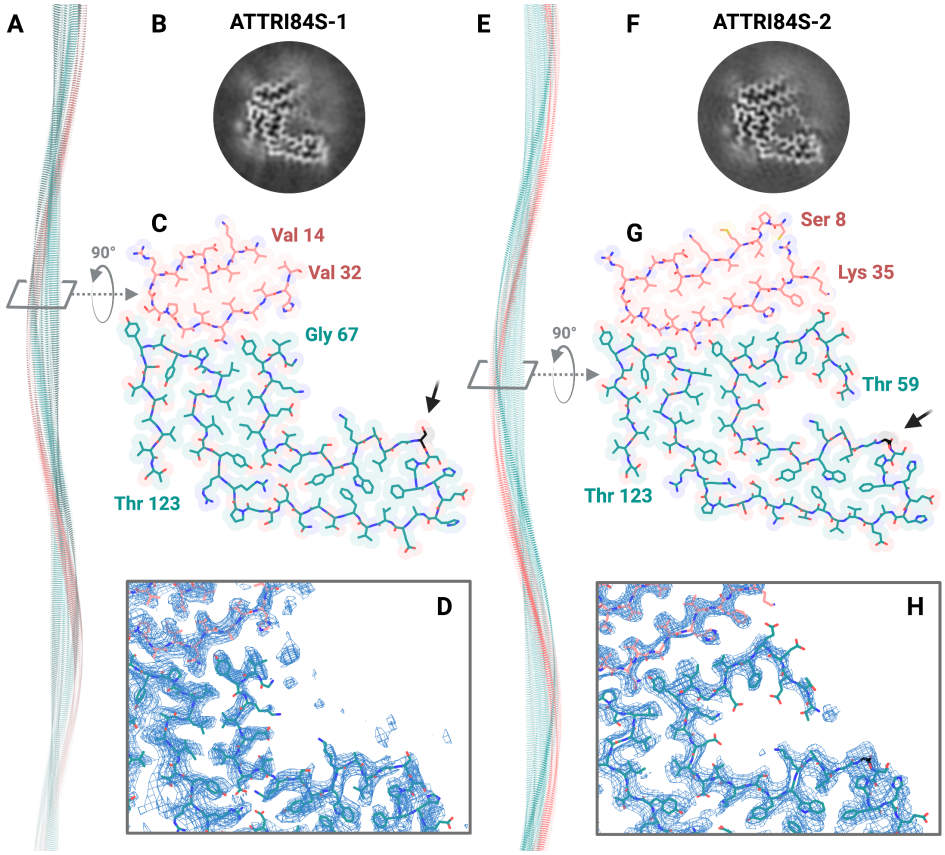

Figure 4. Cryo-EM structures of ATTRI84S fibrils from two patients, ATTRI84S-1 (A-D) and ATTRI84S-2 (E-H). A and E. Model reconstructions. The N terminal fragment of transthyretin is colored pink, and the C terminal is colored turquoise. **B and F.** 3D class averages. **C and G.** Atomic model of ATTRI84S fibrils, as labeled. The N terminal fragment of transthyretin is colored pink, and the C terminal is colored turquoise. Arrows point at the mutation site. **D and H.** Close view of the cryo-EM density and atomic model of the polar channel in ATTRI84S fibrils.

ATTRv mutations are associated with fibril density perturbations.

A close examination of the density maps of ATTR structures reveals additional differences between ATTRwt and ATTRv fibrils. The local resolution maps indicate structural perturbations in ATTRv fibrils that are not apparent in the model reconstruction (Figure 5). These structural perturbations influence the local resolution of the density maps at and near ATTRv mutations. In ATTRP24S and ATTRI84S-1 fibrils, the resolution near the mutation sites reaches ~6.5 Å and the overall map resolutions are 3.65 and 3.61 Å, respectively. In ATTRI84S-2 fibrils, the resolution near the mutation site reaches ~3.8 Å, and the overall map resolution is 3.07 Å. In ATTRV122I and ATTRT60A fibrils, the structural perturbation affects the surface of the fibril rather than the mutation site only. The resolution at the surface of the two types of ATTRV122I fibrils reaches ~4.2 Å, and the overall resolution of their maps is 3.16 and 3.2 Å. In ATTRT60A fibrils, the resolution at the surface reaches ~3.8 Å, and the overall resolution is 3.3 Å. In contrast, the resolution map of ATTRwt fibrils is more homogeneous.

A

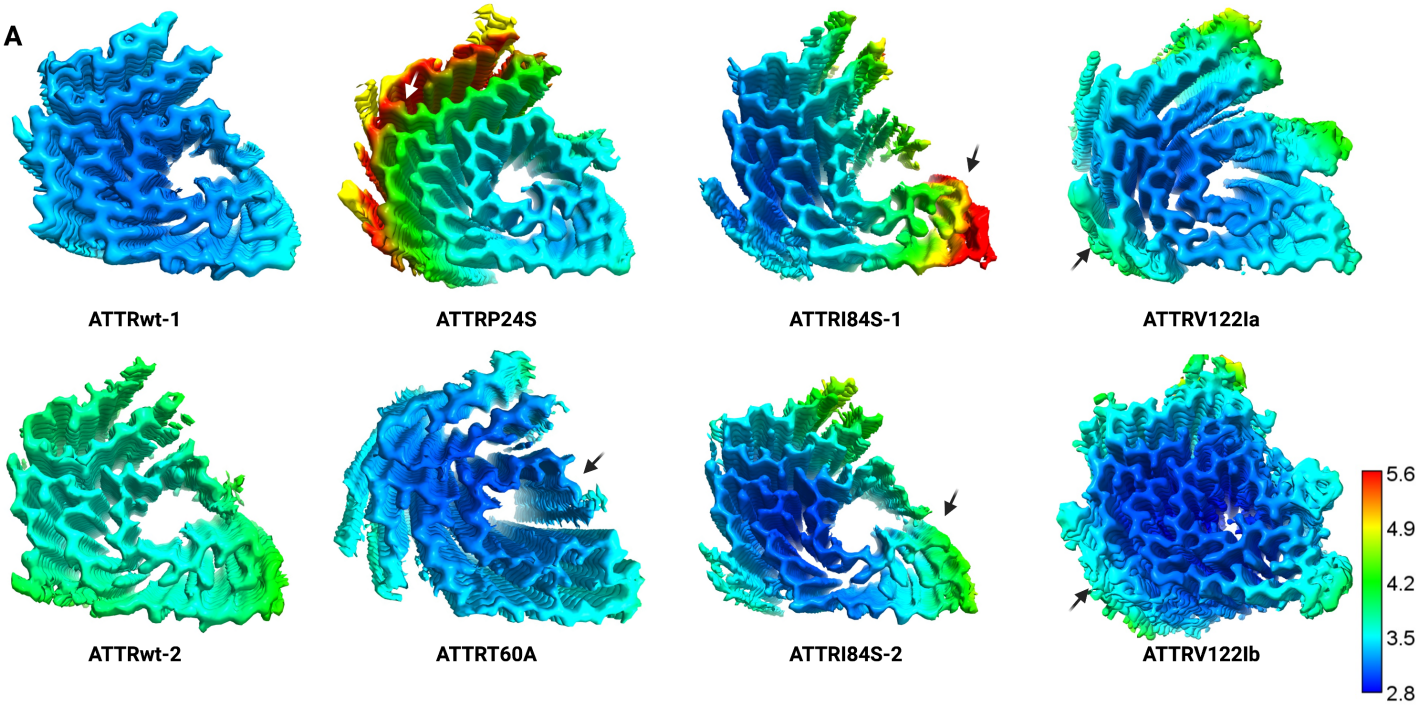

B

Resolution (Å)	wt-1	wt-2	P24S	T60A	I84S-1	I84S-2	V122Ia	V122Ib
Overall	3.31	3.70	3.65	3.30	3.61	3.07	3.16	3.20
Maximum	3.08	3.57	3.22	3.00	3.02	2.94	3.03	3.01
Minimum	3.37	4.60	6.67	3.81	6.27	3.82	4.42	4.18

Figure 5. Local resolution maps of ATTR fibrils. A. Local resolution estimation for 3D reconstructions of ATTR fibrils. Arrows point to the locations of mutations on each density map. ATTRP24S mutation is marked with a white arrow to facilitate color contrast. Resolution scale in Angstroms. **B.** Summary of overall, maximum, and minimum resolution values of ATTR fibril maps shown in **A**.

ATTR fibrils are exceptionally stable.

Both ATTRwt and ATTRv fibrils proved extremely stable (Figure 6). The free energy of these fibrils per chain ranges from –49.1 and –66.9 kcal/mol (Figure 6A). We compared their thermodynamic stability to the amyloid structures reported in the Amyloid Atlas by January 2022 and found that ATTR fibrils are significantly more stable than other fibrils, both by residue and chain (Figure 6B)[14,15]. Analysis by residue reveals that the stability of ATTR fibrils results from the contribution of three pockets—the inner interface of the hairpin formed between Val 14 and Val 32, the inner pocket of the arch formed between residues Trp 79 and Phe 95, and the triquetra that connects the C and N terminal fragments together (Figure 6C). Most ionizable residues of ATTR fibrils are exposed to the outside, thereby enabling neutralization by other interactions that also contribute to the fibril stability. These include π-π stacking of aromatic residues (Figure 6D), hydrogen bonding from the stacking of asparagines along the fibril (Figure 6E), and hydrogen bonding of exposed ionizable residues within the same chain (Figure 6F). It is worth noting that the loss of the C-terminal segment ending in Gly 67 in ATTRI84S-1 fibrils does not seem to affect the overall stability of the fibril (-54.4 kcal/mol), which is comparable to the other ATTR structures (Figure 6A).

A

	wt-1	wt-2	P24S	T60A	I84S-1	I84S-2	V122Ia	V122Ib	V30M 7ob4	V30M 6sdz
Per chain	-59.0	-58.0	-56.4	-66.9	-54.4	-49.1	-57.4	-60.8	-62.4	-62.1
Per residue	-0.64	-0.63	-0.62	-0.73	-0.68	-0.53	-0.64	-0.62	-0.68	-0.68

ΔG_o(kcal/mol)

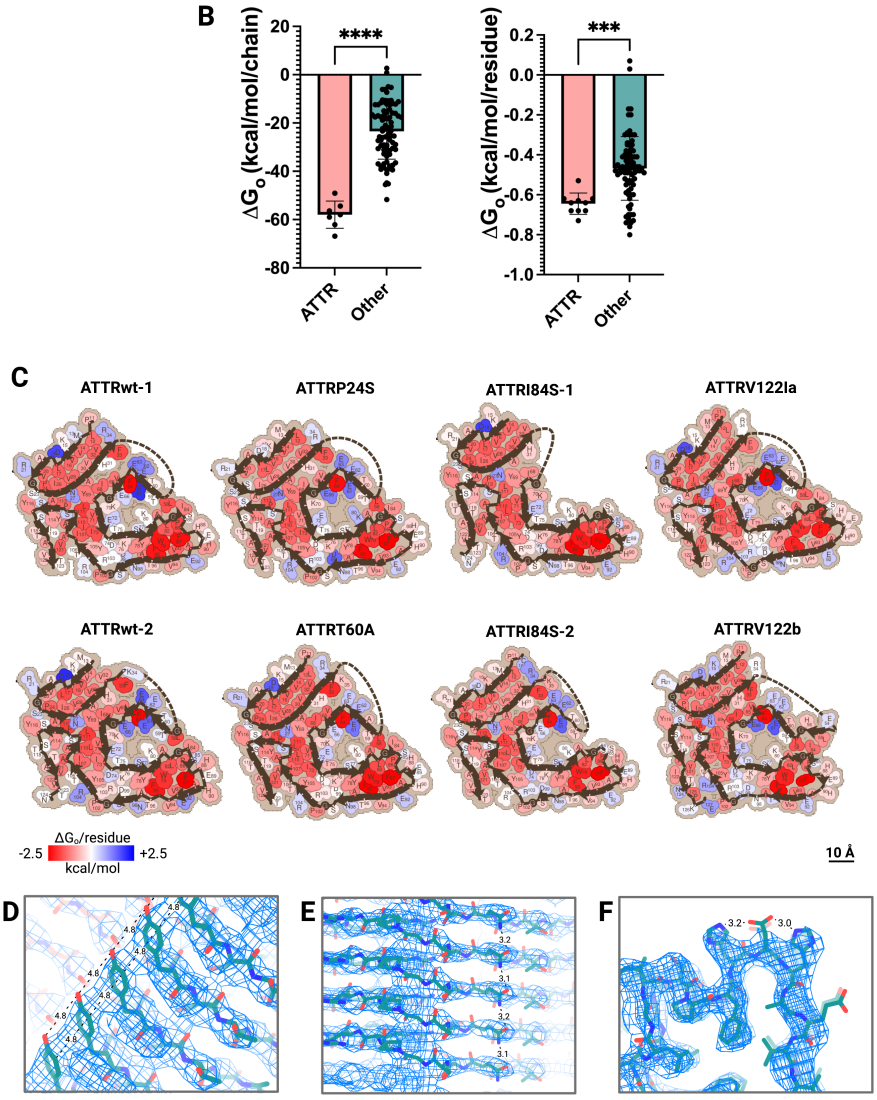

Figure 6. Fibril stability in ATTR amyloidosis. A. Stabilization energies per chain and per residue of ATTR fibrils in kcal/mol. **B.** Comparison of stabilization energies between ATTR fibrils and all amyloid fibrils reported in the Amyloid Atlas 2022[14]. Left, stabilization energies by chain. Right, stabilization energies by residue. ATTR fibrils are significantly more stable than the other amyloid structures, considering the energies of both chains and residues. ***, p<0.001; ****, p<0.0001. **C.** Representation of stabilization energies per residue of cardiac ATTR fibrils determined in this study. Strongly stabilizing side chains are colored red, and destabilizing side chains are colored blue. **D, E and F.** Ionizable side chains on the outside of ATTR fibrils can be neutralized by π-π stacking **(D)**, hydrogen bonding stacking **(E)**, or intra-chain hydrogen bonding **(F)**. These three panels show examples found in ATTRwt-1 fibrils.

Discussion

Our study reveals that ATTR fibrils are polymorphic and challenge the connection of distinct amyloid diseases to distinct fibril polymorphs. Tau fibrils in tauopathies and α-synuclein fibrils in synucleinopathies exhibit distinct structural folds linked to distinct diseases[9,16,17]. Unlike in these diseases, our studies reveal that cardiac fibrils from various patients of ATTR amyloidosis exhibit structural heterogeneity at several levels (Figure 7). We found conformational polymorphism in fibrils from two independent patients carrying the same ATTRI84S mutation (Figure 4), and polymorphism in the fold and the twist of ATTRV122I fibrils extracted from the same patient (Figure 3). We also found that the structure of ATTRv fibrils exhibits local resolution perturbations in resolution whereas the resolution of ATTRwt fibrils is homogeneously dispersed (Figure 5). These findings suggest that the structural heterogeneity in ATTR amyloidosis varies from patient to patient, instead of being specific to the disease (Figure 3C).

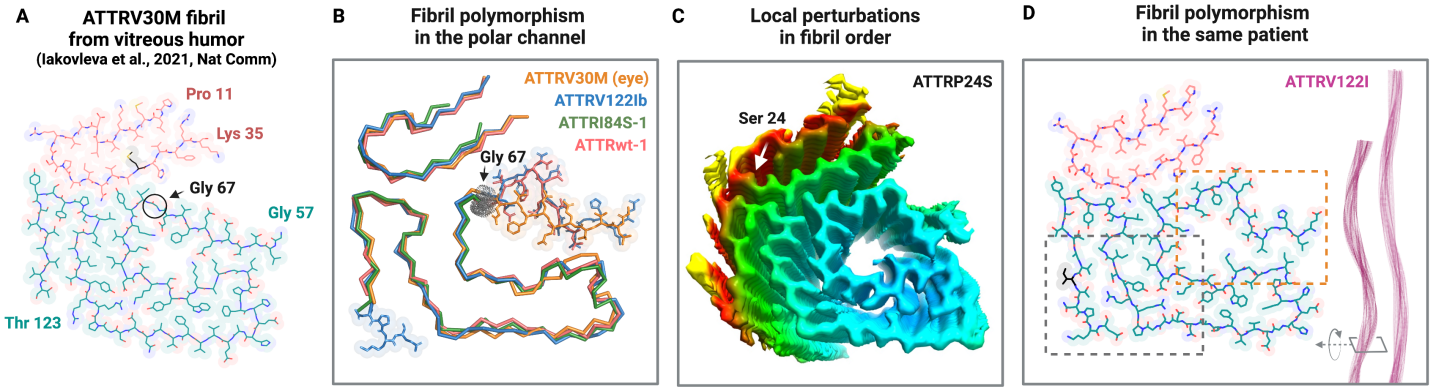

Figure 7. Fibril polymorphism in ATTR amyloidosis. A. Cryo-EM model reconstruction of one of the two protofilaments present in ATTRV30M fibrils from vitreous humor[12]. The C terminal segment is colored pink. The N terminal segment is colored turquoise. The segment Gly 57 to Gly 67 crosses the polar channel diagonally, instead of in the shape of a pentagon. **B, C, and D.** ATTR fibril heterogeneity is structurally manifested at several levels. **B.** The segment that ends at Gly 67 folds differently in several ATTR fibril structures. For instance, in ATTRV30M fibrils from vitreous humor, this segment crosses the channel diagonally (blue). In ATTRI84S fibrils, this segment can be found surrounding the channel with the shape of a pentagon (red) or be disordered (green). **C.** Some ATTR mutations, such as ATTRP24S shown in this panel, display local resolution perturbations that may be associated with structural disorder. **D.** ATTRV122I fibrils deposit in two conformations that differ in fibril twist and the presence or absence of a protein stretch that contains the last four residues of transthyretin (dashed square).

Our findings challenge the current paradigm of “one disease equals one fibril polymorph,” and it remains to be seen whether similarly novel conformations occur in other amyloidoses. In contrast to ATTRv fibrils, we found that ATTRwt fibrils extracted from two independent patients are structurally equivalent, sharing the same fold and lacking local order perturbations (Figure 1, 5, and Supplementary Figure 3). Since all *ex-vivo* fibril structures determined to date depict wild-type sequences, with the exception of the two ATTR fibril structures described prior to our study[9,16,18–23], we expect that familial mutations of tau or α-synuclein, for instance, could lead to novel conformations.

This new perspective challenges the origins of amyloid diseases and their connection to fibril polymorphism. There are two hypotheses that explain the origins of amyloid diseases[15]. The "polymorph-first" hypothesis states

that fibril nucleation precedes and steers disease manifestation. The “disease-first” hypothesis implies that each disease is associated with a cell environment that leads to the formation of a particular polymorph. Both hypotheses are based on the paradigm that all patients of a particular disease are associated with the same fibril fold(s). Our results show that patients with the same disease and genotype and even the same patient can associate with two, or perhaps more, polymorphs. Consequently, neither of the two hypotheses could explain the origins of ATTR amyloidosis, unless all the phenotypic complexity of ATTR amyloidosis is decomposed into various independent diseases, each associated with a particular fibril polymorph/s. A more comprehensive study of ATTR fibril structures and their association with clinical presentation could resolve this conundrum.

Several studies suggest a potential connection of ATTR amyloid fibril polymorphism with clinical presentation. Histopathological studies of ATTR fibrils reveal two distinct fibril types: type A, composed of full-length and fragmented transthyretin, and type B, composed exclusively of full-length transthyretin[24]. The samples used for cryo-EM structure reconstruction in this paper contain type A fibrils[25]. Type A and B fibrils are associated with differential clinical presentations in ATTRV30M amyloidosis patients[24]. We showed that the presence of fragmented transthyretin in ATTR fibril extracts has a positive correlation with their potential to seed further fibril formation[25]. Consistently, Type B ATTR patients have delayed cardiac deposition of wild-type transthyretin after liver transplantation than do Type A ATTR patients, who develop rapid cardiac deposition post-surgery[26,27]. The structural variability that we found in ATTR fibrils indicates that type A pathology can consist of structural polymorphs, but with the limited information we have about the phenotypes of these patients, little can be said about the implications of our findings in pathology.

The analysis of ATTR fibril stability reveals unexpected observations and informs us about transthyretin amyloidogenesis. Compared to other amyloid fibrils[14], ATTR fibrils exhibit the greatest stability measured to date (Figure 7). As discussed by Sawaya et al., the great stability of the amyloid structure is driven by the power of backbone hydrogen bonding, or *cross-β scaffolds*, and reinforced by the interdigitation of sidechains projecting from the faces of two mated β-sheets, or *steric zipper motifs*[15]. In ATTR fibrils, the steric zipper motifs bring together three hydrophobic pockets that are the main contributors to the extraordinary stability of these fibrils. These are two β-arches (Val 14 to Val 32 and Trp 79 to Phe 95) and a hydrophobic triquetra that connects the C and N terminal fragments (Figure 7C). The cross-β scaffolding allows for the interaction of neighboring aliphatic and aromatic residues through Van der Waals contacts and π-π stacking. In ATTR fibrils, we see many examples of π-π interactions from the stacking of aromatic residues that contribute to the stability of the fibrils (Figure 7D). Another source of fibril stability is the hydrogen bonding that results from the stacking of Asn 27, Asn 98, and Asn 123 along the fibril (Figure 7E). Exposure of most of the ionizable residues to the outside of the ATTR fibril or into the polar channel allows for the neutralization of their charges by posttranslational modifications, or hydrogen bonding with waters and ligands (Figure 7F-G). This extraordinary fibril stability likely results in greater resistance to proteolysis, denaturation, and clearance.

The outstanding structural stability across all ATTR fibrils, including from ATTRwt patients, substantiates the notion that ATTRv mutations accelerate disease onset by decreasing the dissociation energy barrier of transthyretin tetramers, rather than promoting fibril formation[28,29]. Although we observed that mutations cause structural perturbations in fibrils, we found that the stability of ATTRv fibrils does not differ from the stability of ATTRwt fibrils (Figure 7), suggesting that the role of the mutations is more likely attributed to lowering the kinetic barrier to amyloid fibril formation, rather than stabilizing the fibril itself. This may explain why ATTRv fibrils are composed of both wild-type and variant transthyretin, given that both contribute to the stability of the fibril in a similar fashion. We imagine that after initial nucleation and elongation of ATTRv, wild-type monomers of transthyretin can be incorporated into the fibril by seeding[25].

Our study suggests that this process of monomer addition during polymerization or seeding does not involve the polar channel, whose formation may not be necessary for amyloidogenesis and/or pathogenesis. We found that ATTR fibrils exhibit conformational variability in the polar channel, through segment Gly 57 to Gly 67, without

affecting ATTR fibril stability significantly (Figure 6). In ATTRwt, ATTRP24S, ATTRT60A, and ATTRV122I fibrils, this segment surrounds and closes a polar channel that encompasses residues Gly 57 to Ile 84 (Figures 1, 2, and 3). Schmidt et al. described that in ATTRV30M cardiac fibrils, this segment adopts the same conformation[11]. Iakovleva et al. showed that in ATTRV30M fibrils extracted from vitreous humor, this segment acquires an alternative fold that crosses the polar channel diagonally (Figure 7A)[12]. In ATTRI84S fibrils from one patient but not from another one, we found that this segment appears disordered (Figure 4). In all these cases, the pivotal residue Gly 67 governs the conformational polymorphism of ATTR fibrils, opening or closing the polar channel. Like ATTR fibrils, many other amyloid fibrils have polar channels that are big enough to fit a wide variety of molecules including globular proteins, and could potentially act as a transporting duct[30]. However, the absence of the polar channel in the fibril structure in one ATTRI84S patient but not in a second one suggests that the formation of this channel and its potential transporting role is not necessary for amyloidogenesis and/or pathogenesis.

The ATTR structural heterogeneity challenges the current concept of amyloid polymorphism. Amyloid polymorphism often refers to different amyloid folds that are adopted by closely identical protein sequences[15]. The structural differences observed in ATTRI84S fibrils agree with this definition, since both ATTRI84S-1 and ATTRI84S-2 fibrils contain the same protein sequence and yet adopt different folding patterns (Figure 4). The two types of ATTRV122I fibrils obtained from the same patient can also be classed as polymorphs, since they have the same sequence but exhibit a different helical twist angle between successive layers within the fibril (Figure 3). The two ATTRV122I fibril types also display subtle changes in the folding, with additional C-terminal amino acids in the ATTRV122Ib fibrils, which have the fastest twisting (Figure 3D-E). However, the changes in the local resolution found in ATTR fibrils may not agree with this definition of polymorphism. We observe that the resolution of the ATTRwt structures is homogeneous throughout the fibril cross-section, suggesting that all the molecules are similarly ordered within the fibril (Figure 5). In ATTRv fibrils, in contrast, we observe local perturbations of the molecular order that coincide with the mutation site (ATTRP24S and ATTRI84S fibrils) or appear at the surface of the fibrils (ATTRT60A and ATTRV122I fibrils). Pending revising the current definition, these perturbations could be defined as polymorphs, if one considers local disorder as a source of polymorphism.

Conclusions

By solving the molecular structures of ex vivo ATTR fibrils from 5 different ATTR genotypes, including wild type ATTR, our study serves as the most comprehensive structural account of ATTR amyloidosis to date. We observe that heterogeneities in the fibril structure exist at local levels of fibril folds, crossover distances, and folds amongst different ATTR mutations. These variations can be between patients, as observed in ATTRI84S fibrils, or exist within the same patient, as with ATTRV122I fibrils. While more information is needed to fully grasp the implications of these findings, our studies highlight the high variability of this disease. Any correlation that exists between the disease phenotype and fibril polymorphs will require wider sampling of fibrils from other mutations and organs. Understanding the phenotype-polymorph relationship might enable expeditious translation of research discoveries into patient-specific diagnostics and therapeutics for amyloidosis.

Materials and Methods

Patients and tissue material. Tissues from ATTR patients carrying wild-type TTR (*n* = 2) or TTR mutations (*n* = 5) included in the study are listed in Supplementary Table 1. Specimens from the left ventricle of either explanted or autopsied hearts were obtained from the laboratory of Dr. Merrill D. Benson at the University of Indiana. The Office of the Human Research Protection Program granted exemption from Internal Review Board review because all specimens were anonymized.

Extraction of amyloid fibrils from human cardiac tissue. *Ex-vivo* preparations of amyloid fibrils were obtained from lyophilized fibrillar extracts or fresh-frozen human tissue as described earlier[11]. The lyophilized fibrillar extracts were collected using the classical method developed by Pras et al. and modified by Westermark et al. years later[31,32]. Both types of specimens were processed using the same method. Briefly, ~200 mg of frozen cardiac tissue per patient was thawed at room temperature and cut into small pieces with a scalpel. The minced tissue or ~100 mg of lyophilized fibrillar extract was suspended into 1 mL Tris-calcium buffer (20 mM Tris, 138 mM NaCl, 2 mM $CaCl_2$, 0.1% NaN_3, pH 8.0) and centrifuged for 5 min at 3100 × g and 4 °C. The pellet was washed in Tris-calcium buffer four additional times. After the washing, the pellet was resuspended in 1 mL of 5 mg/mL collagenase solution (collagenase was dissolved in Tris-calcium buffer) and incubated overnight at 37 °C, shaking at 400 rpm. The resuspension was centrifuged for 30 min at 3100 × g and 4 °C and the pellet was resuspended in 1 mL Tris–ethylenediaminetetraacetic acid (EDTA) buffer (20 mM Tris, 140 mM NaCl, 10 mM EDTA, 0.1% NaN_3, pH 8.0). The suspension was centrifuged for 5 min at 3100 × g and 4 °C, and the washing step with Tris–EDTA was repeated nine additional times. Up to this point, all the supernatants were collected for further analysis, when needed. After the washing, the pellet was resuspended in 200 µL ice-cold water supplemented with 5-10 mM EDTA and centrifuged for 5 min at 3100 × g and 4 °C. This step released the amyloid fibrils from the pellet, which were collected in the supernatant. EDTA helped solubilize the fibrils. This extraction step was repeated five additional times. The material from the various patients was handled and analyzed separately.

Negative-stained transmission electron microscopy. Amyloid fibril extraction was confirmed by transmission electron microscopy as described[33]. Briefly, a 3 µL sample was spotted onto a freshly glow-discharged carbon-coated grid (Ted Pella), incubated for 2 min, and gently blotted onto a filter paper to remove the solution. The grid was negatively stained with 5 µL of 2% uranyl acetate for 2 min and gently blotted to remove the solution. Another 5 µl uranyl acetate was applied onto the grid and immediately removed. An FEI Tecnai 12 electron microscope at an accelerating voltage of 120 kV was used to examine the specimens.

Cryo-EM sample preparation, data collection, and processing. Freshly extracted fibril samples were applied to glow-discharged Quantifoil R 1.2/1.3, 300 mesh, Cu grids, blotted with filter paper to remove excess sample, and plunged frozen into liquid ethane using a Vitrobot Mark IV (FEI). Cryo-EM samples were screened on either the Talos Arctica or Glacios at the Cryo-Electron Microscopy Facility (CEMF) at University of Texas Southwestern Medical Center (UTSW), and the final datasets were collected on a 300 kV Titan Krios microscope (FEI) at three different facilities: the CEMF, the Pacific Northwest Center for Cryo-EM (PNCC), and the Stanford-SLAC Cryo-EM Center (S^2C^2) (Supplementary Table 2). Pixel size, frame rate, dose rate, final dose, and number of micrographs per sample are detailed in Supplementary Table 2. Automated data collection was performed by SerialEM software package[34].

The raw movie frames were gain-corrected, aligned, motion-corrected and dose-weighted using RELION's own implemented motion correction program[35]. Contrast transfer function (CTF) estimation was performed using CTFFIND 4.1[36]. All steps of helical reconstruction, three-dimensional (3D) refinement, and post-process were carried out using RELION 3.1[37].

All filaments were manually picked using EMAN2 e2helixboxer.py[38]. Particles were first extracted using a box size of 1024, and 256 pixels with an inter-box distance of 10% of the box length. 2D classification of 1024-pixel particles was used to estimate the helical parameters. 2D classifications of 256-pixel particles were used to select suitable particles for further processing. Fibril helix is assumed to be left-handed. We performed 3D classifications with the average of ~30k to 40k particles per class to separate filament types using an elongated Gaussian blob as an initial reference. Particles potentially leading to the best reconstructed map were chosen for 3D auto-refinements. CTF refinements and Bayesian polishing were performed to obtain higher resolution. Final maps were post-processed using the recommended standard procedures in RELION. The final subset of selected particles was used for high-resolution gold-standard refinement as described previously[39]. The final

overall resolution estimate was evaluated based on the FSC at 0.143 threshold between two independently refined half-maps[40].

Model building. The refined maps were further sharpened using phenix.auto_sharpen at the resolution cutoff[41]. Previously published model of ATTR-V30M (pdb code 6SDZ) was used as the template to build all near atomic resolution models. Mutations, rigid body fit zone, and real space refine zone were performed to obtain the resulting models using COOT[42]. All the statistics are summarized in Supplementary Table 2.

Stabilization energy calculation. The stabilization energy per residue was calculated by the sum of the products of the area buried for each atom and the corresponding atomic solvation parameters (Supplementary Figure 5). The overall energy was calculated by the sum of energies of all residues, and assorted colors were assigned to each residue, instead of each atom, in the solvation energy map.

Recombinant protein expression and purification. Recombinant protein samples were prepared as described previously[33]. Briefly, monomeric transthyretin (MTTR) was expressed in *Escherichia coli* and purified by affinity in a HisTrap column (GE Healthcare Life Science). Peak fractions were combined and further purified by size exclusion chromatography on a Superdex S75 prep grade column (GE Healthcare Life Science) in sodium phosphate–EDTA buffer (10 mM sodium phosphate pH 7.5, 100 mM KCl, and 1 mM EDTA). Peak fractions were pooled and stored at −20 °C.

Amyloid Seeding Assays. Amyloid fibril extracts were used to seed the formation of new fibrils from recombinant MTTR as we described previously[25]. Briefly, we further purified the extracts by treatment with 1% sodium dodecyl sulfate in NaP-EDTA buffer and centrifugation at 13,000 rpm for 10 min (rotor FA-24x2, Eppendorf). This purification process was repeated two times, and soluble fractions were discarded. The sample was washed with NaP-EDTA buffer three times by centrifugation and sonicated in cycles of 5 seg on/5 seg off for a total of 10 min at the minimum intensity (18%). The total protein content in the seed preparation was measured by the Pierce BCA Protein Assay Kit (Thermo Fisher Scientific). 2% (w/w) seeds were added to 0.5 mg/mL recombinant MTTR in a final volume of 200 µL containing 5 µM thioflavin T (ThT) and 1x PBS (pH 7.4). ThT fluorescence emission was measured at 482 nm with absorption at 440 nm in a FLUOstar Omega (BMG LabTech) microplate reader. Plates were incubated at 37 °C with cycles of 9 min shaking (700 rpm double orbital) and 1 min rest throughout the incubation. Measurements were taken every 10 min (bottom read) with a manual gain of 1,000. Figures show ThT signal in relative fluorescence units (RFU). Fibril formation was confirmed by transmission electron microscopy.

Statistical Analysis. Statistical analysis of fibril stability was performed with Prism 9 for Mac (GraphPad Software) using an unpaired t test. All samples were included in the analysis and all measurements are displayed in the graphs.

Data and Materials Availability.

Structural data have been deposited into the Worldwide Protein Data Bank (wwPDB) and the Electron Microscopy Data Bank (EMDB) with the following EMD accession codes: 26587, 26685, 26688, 26691, 26692, 27323, 27324, 27325. The PDB accession codes for the previously reported coordinates of ATTRV30M fibrils from vitreous humor and heart are 7ob4 and 6sdz, respectively. All data generated or analyzed during this study that support the findings are available within this published article and its supplementary data files.

Acknowledgments

In memory of Late Dr. Merrill D. Benson, who contributed greatly to the understanding of amyloid diseases and helped affected families for decades. We thank Justyna Kurleto, Morgan Schackmuth, and Drs. Romany Abskharon and Barbara Kluve-Beckerman for their technical support and useful discussion. We thank Aline McKensie for manuscript editing. Special thanks to the patients and families who generously donated tissues. We thank the UTSW Cryo-Electron Microscopy Facility, the UTSW Structural Biology Laboratory, the UTSW Electron Microscopy Core Facility, the UCLA California NanoSystems Institute, and the national cryo-EM facilities Stanford-SLAC (project CA60), PNCC (project 51267), and National Center for Cryo-EM Access and Training (NCCAT) for instrumentation, technical support, and/or data collection. Finally, we thank all the Twitter users that reconciled our scientific dilemma about the shape of our ATTR fibril (Twitter Poll.)

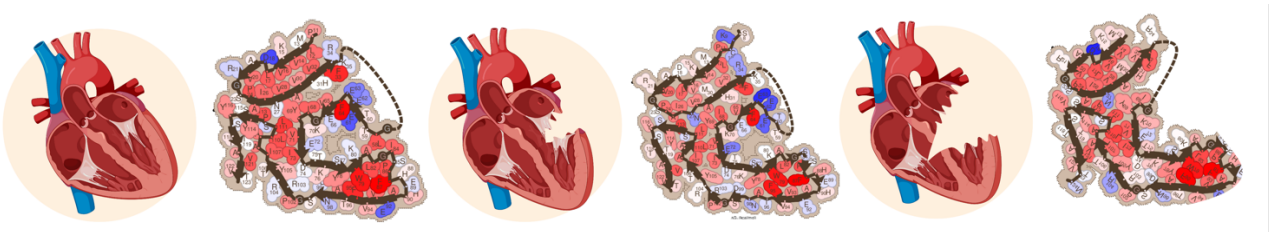

Funding

This research was supported in part by the American Heart Association (Career Development Award 847236), the NIH National Heart, Lung, and Blood Institute (New Innovator Award DP2-HL163810), the NIH National Institute on Aging (RF1-AG048120), the Welch Foundation (Research Award I-2121-20220331), and the UTSW Endowment (Distinguished Researcher Award from President's Research Council and start-up funds). Cryo-EM research was partially supported by (1) NIH grant U24GM129547 and performed at the PNCC at OHSU and accessed through EMSL (grid.436923.9), a Department of Energy Office of Science User Facility sponsored by the Office of Biological and Environmental Research; (2) the Department of Energy, Laboratory Directed Research and Development program at SLAC National Accelerator Laboratory, under contract DE-AC02-76SF00515; and (3) the NIH Common Fund Transformative High Resolution Cryo-Electron Microscopy program (U24 GM129539,) and by grants from the Simons Foundation (SF349247) and NY State Assembly and accessed through the NCCAT and the Simons Electron Microscopy Center located at the New York Structural Biology Center. The Cryo-Electron Microscopy Facility and the Structural Biology Laboratory at UTSW are supported by a grant from the Cancer Prevention & Research Institute of Texas (RP170644). The Electron Microscopy Core Facility at UTSW is supported by the National Institutes of Health (NIH) (1S10OD021685-01A1 and 1S10OD020103-01). Part of the computational resources were provided by the BioHPC supercomputing facility located in the Lyda Hill Department of Bioinformatics at UTSW. URL: https://portal.biohpc.swmed.edu.

Conflicts interests. None.

References

1. Eisenberg, D. & Jucker, M. The amyloid state of proteins in human diseases. *Cell* **148**, 1188-1203 (2012).
2. Riek, R. & Eisenberg, D. S. The activities of amyloids from a structural perspective. *Nature* **539**, 227-235 (2016).
3. Hamilton, J. A. & Benson, M. D. Transthyretin: a review from a structural perspective. *Cell Mol Life Sci* **58**, 1491-1521 (2001).
4. Ando, Y. et al. Guideline of transthyretin-related hereditary amyloidosis for clinicians. *Orphanet J Rare Dis* **8**, 31 (2013).
5. Galant, N. J., Westermark, P., Higaki, J. N. & Chakrabartty, A. Transthyretin amyloidosis: an under-recognized neuropathy and cardiomyopathy. *Clin Sci (Lond)* **131**, 395-409 (2017).
6. Falcon, B. et al. Structures of filaments from Pick's disease reveal a novel tau protein fold. *Nature* **561**, 137-140 (2018).
7. Falcon, B. et al. Tau filaments from multiple cases of sporadic and inherited Alzheimer's disease adopt a common fold. *Acta Neuropathol* **136**, 699-708 (2018).
8. Falcon, B. et al. Novel tau filament fold in chronic traumatic encephalopathy encloses hydrophobic molecules. *Nature* **568**, 420-423 (2019).
9. Schweighauser, M. et al. Structures of α-synuclein filaments from multiple system atrophy. *Nature* **585**, 464-469 (2020).
10. Scheres, S. H., Zhang, W., Falcon, B. & Goedert, M. Cryo-EM structures of tau filaments. *Curr Opin Struct Biol* **64**, 17-25 (2020).
11. Schmidt, M. et al. Cryo-EM structure of a transthyretin-derived amyloid fibril from a patient with hereditary ATTR amyloidosis. *Nat Commun* **10**, 5008 (2019).
12. Iakovleva, I. et al. Structural basis for transthyretin amyloid formation in vitreous body of the eye. *Nat Commun* **12**, 7141 (2021).
13. Nelson, R. et al. Structure of the cross-beta spine of amyloid-like fibrils. *Nature* **435**, 773-778 (2005).
14. Sawaya, M. R. Amyloid Atlas 2022. (2022).
15. Sawaya, M. R., Hughes, M. P., Rodriguez, J. A., Riek, R. & Eisenberg, D. S. The expanding amyloid family: Structure, stability, function, and pathogenesis. *Cell* **184**, 4857-4873 (2021).
16. Shi, Y. et al. Structure-based classification of tauopathies. *Nature* **598**, 359-363 (2021).
17. Shahnawaz, M. et al. Discriminating α-synuclein strains in Parkinson's disease and multiple system atrophy. *Nature* **578**, 273-277 (2020).
18. Yang, Y. et al. Cryo-EM structures of amyloid-β 42 filaments from human brains. *Science* **375**, 167-172 (2022).
19. Radamaker, L. et al. Cryo-EM structure of a light chain-derived amyloid fibril from a patient with systemic AL amyloidosis. *Nat Commun* **10**, 1103 (2019).
20. Radamaker, L. et al. Cryo-EM reveals structural breaks in a patient-derived amyloid fibril from systemic AL amyloidosis. *Nat Commun* **12**, 875 (2021).
21. Kollmer, M. et al. Cryo-EM structure and polymorphism of Aβ amyloid fibrils purified from Alzheimer's brain tissue. *Nat Commun* **10**, 4760 (2019).
22. Liberta, F. et al. Cryo-EM fibril structures from systemic AA amyloidosis reveal the species complementarity of pathological amyloids. *Nat Commun* **10**, 1104 (2019).
23. Swuec, P. et al. Cryo-EM structure of cardiac amyloid fibrils from an immunoglobulin light chain AL amyloidosis patient. *Nat Commun* **10**, 1269 (2019).
24. Ihse, E. et al. Amyloid fibril composition is related to the phenotype of hereditary transthyretin V30M amyloidosis. *J Pathol* **216**, 253-261 (2008).
25. Saelices, L. et al. Amyloid seeding of transthyretin by ex vivo cardiac fibrils and its inhibition. *Proc Natl Acad Sci U S A* **115**, E6741-E6750 (2018).
26. Yazaki, M. et al. Progressive wild-type transthyretin deposition after liver transplantation preferentially occurs onto myocardium in FAP patients. *Am J Transplant* **7**, 235-242 (2007).
27. Ihse, E., Suhr, O. B., Hellman, U. & Westermark, P. Variation in amount of wild-type transthyretin in different fibril and tissue types in ATTR amyloidosis. *J Mol Med (Berl)* **89**, 171-180 (2011).

28. Lashuel, H. A., Lai, Z. & Kelly, J. W. Characterization of the transthyretin acid denaturation pathways by analytical ultracentrifugation: implications for wild-type, V30M, and L55P amyloid fibril formation. *Biochemistry* **37**, 17851-17864 (1998).
29. Cendron, L. et al. Amyloidogenic potential of transthyretin variants: insights from structural and computational analyses. *J Biol Chem* **284**, 25832-25841 (2009).
30. Taylor, A. I. P. & Staniforth, R. A. General Principles Underpinning Amyloid Structure. *Frontier in Neurosicence* **16**, (2022).
31. Pras, M., Schubert, M., Zucker-Franklin, D., Rimon, A. & Franklin, E. C. The characterization of soluble amyloid prepared in water. *J Clin Invest* **47**, 924-933 (1968).
32. Westermark, P., Sletten, K., Johansson, B. & Cornwell, G. G. Fibril in senile systemic amyloidosis is derived from normal transthyretin. *Proc Natl Acad Sci U S A* **87**, 2843-2845 (1990).
33. Saelices, L. et al. Uncovering the mechanism of aggregation of human transthyretin. *J Biol Chem* **290**, 28932-28943 (2015).
34. Mastronarde, D. N. Automated electron microscope tomography using robust prediction of specimen movements. *J Struct Biol* **152**, 36-51 (2005).
35. Zivanov, J., Nakane, T. & Scheres, S. H. W. A Bayesian approach to beam-induced motion correction in cryo-EM single-particle analysis. *IUCrJ* **6**, 5-17 (2019).
36. Rohou, A. & Grigorieff, N. CTFFIND4: Fast and accurate defocus estimation from electron micrographs. *J Struct Biol* **192**, 216-221 (2015).
37. He, S. & Scheres, S. H. W. Helical reconstruction in RELION. *J Struct Biol* **198**, 163-176 (2017).
38. Bell, J. M., Chen, M., Durmaz, T., Fluty, A. C. & Ludtke, S. J. New software tools in EMAN2 inspired by EMDatabank map challenge. *J Struct Biol* **204**, 283-290 (2018).
39. Scheres, S. H. RELION: implementation of a Bayesian approach to cryo-EM structure determination. *J Struct Biol* **180**, 519-530 (2012).
40. Chen, S. et al. High-resolution noise substitution to measure overfitting and validate resolution in 3D structure determination by single particle electron cryomicroscopy. *Ultramicroscopy* **135**, 24-35 (2013).
41. Terwilliger, T. C., Sobolev, O. V., Afonine, P. V. & Adams, P. D. Automated map sharpening by maximization of detail and connectivity. *Acta Crystallogr D Struct Biol* **74**, 545-559 (2018).
42. Emsley, P., Lohkamp, B., Scott, W. G. & Cowtan, K. Features and development of Coot. *Acta Crystallogr D Biol Crystallogr* **66**, 486-501 (2010).

Supplementary Figures

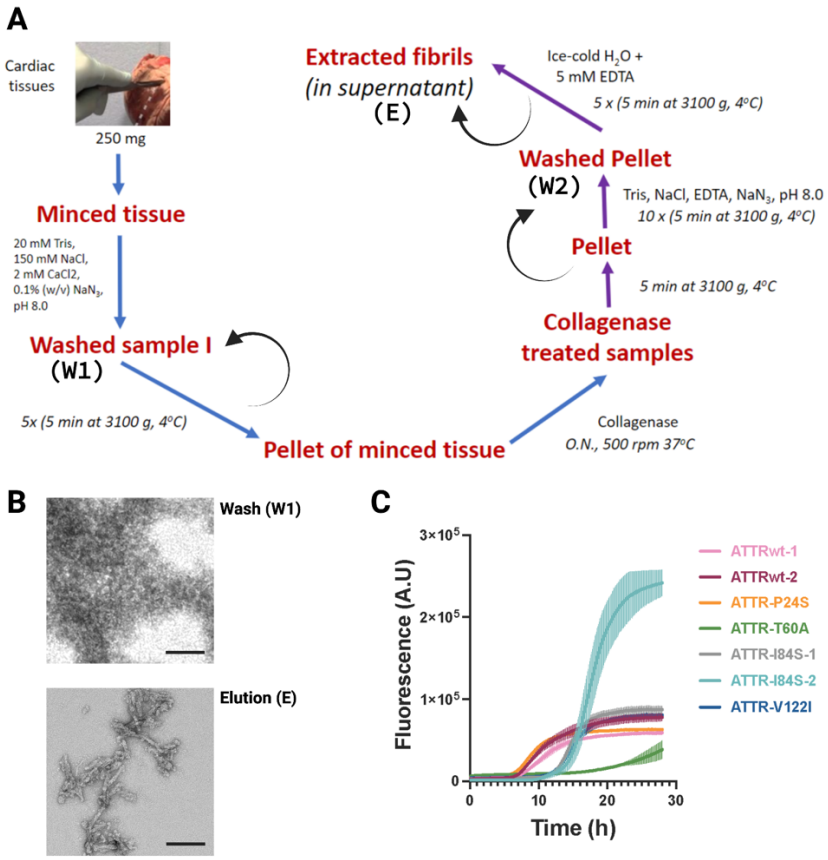

Supplementary Figure 1. Extraction and assessment of ATTR fibrils from cardiac tissue. A. Schematic workflow for ATTR fibril extraction from human heart tissue. **B.** Representative negative stained TEM images of the first wash step (W1) of fibril extraction and the final fibril elution (E). Scale bar, 100 nm. **C.** ThT assay confirming that the fibrillar content of the elution can seed fibril formation of monomeric TTR at pH 7.4.

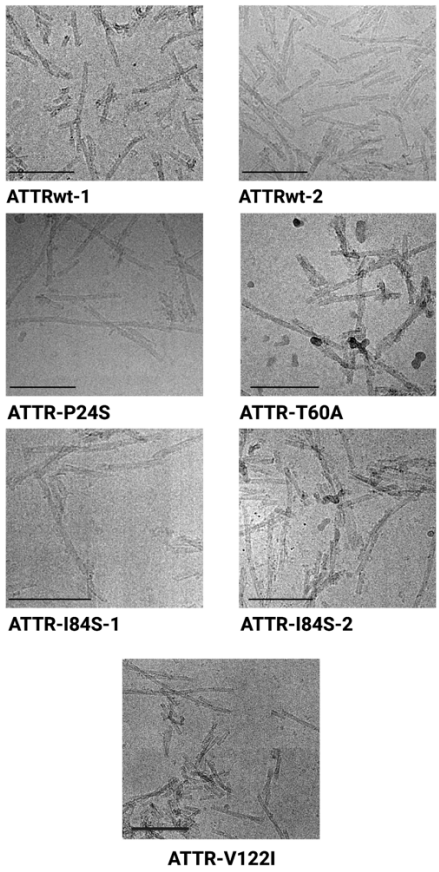

Supplementary Figure 2. Representative cryo-EM micrographs of *ex vivo* cardiac fibrils. Scale bar, 100 nm.

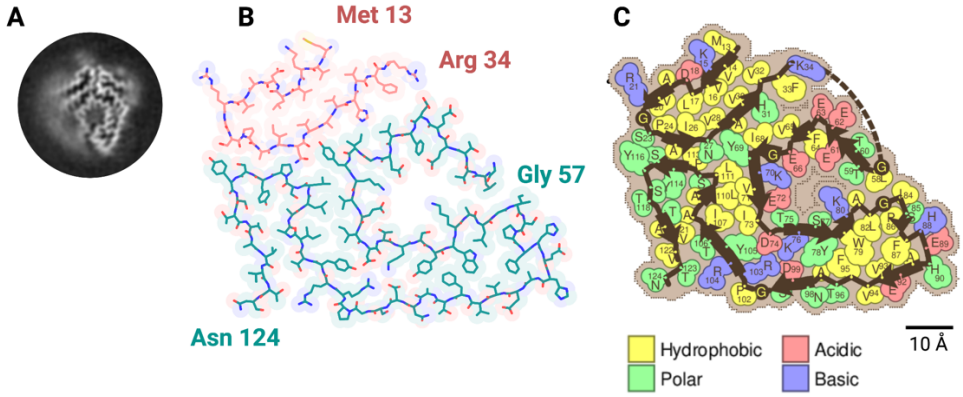

Supplementary Figure 3. Cryo-EM structure of cardiac fibrils from an ATTRwt amyloidosis patient, ATTRwt-2. A. 3D class averages of curvy fibrils. **B.** Cryo-EM density and atomic model. Same as for the patient ATTRw-1, the model contains two fragments of transthyretin colored pink (residues Met 13 to Arg 34) and turquoise (residues Gly 57 to Asn 124). **C.** Schematic view of the fibril core showing residue composition.

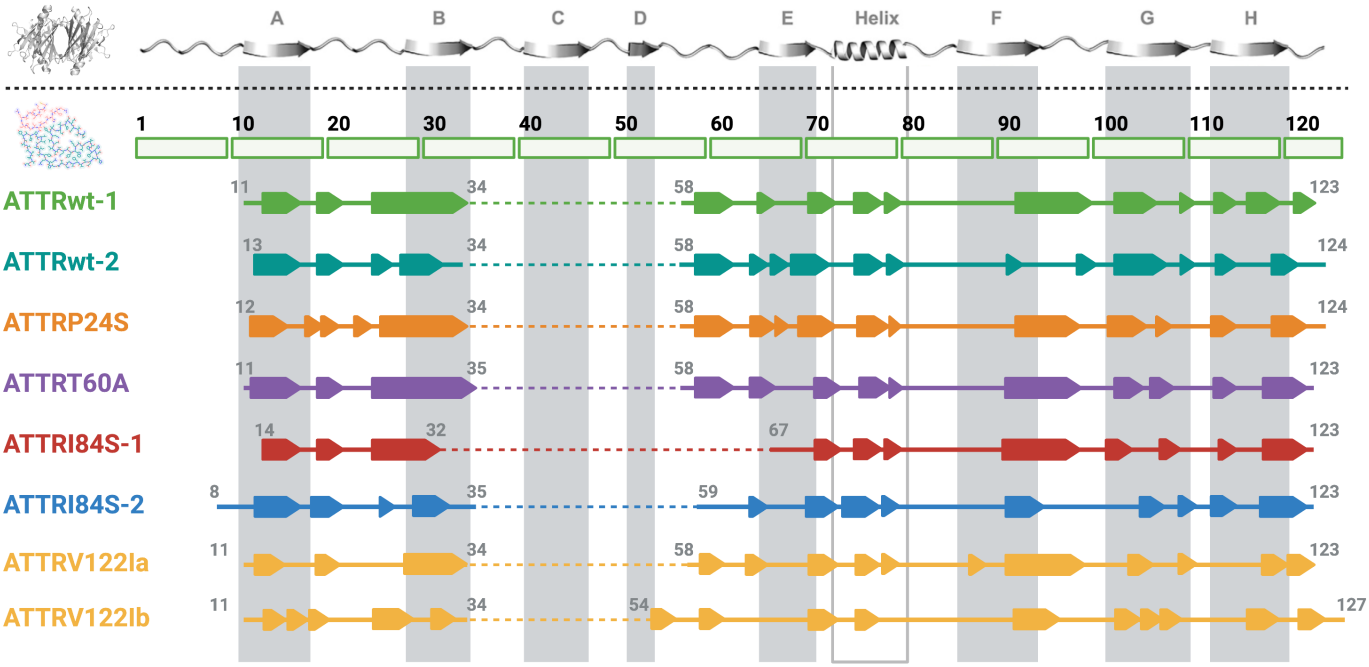

Supplementary Figure 4. Secondary structure composition of ATTR fibrils. Schematic representation of the secondary structure of native transthyretin (above the dashed line) and fibrils from ATTRv and ATTRwt genotypes (below the dashed line). Fibrils are color-coded by patient.

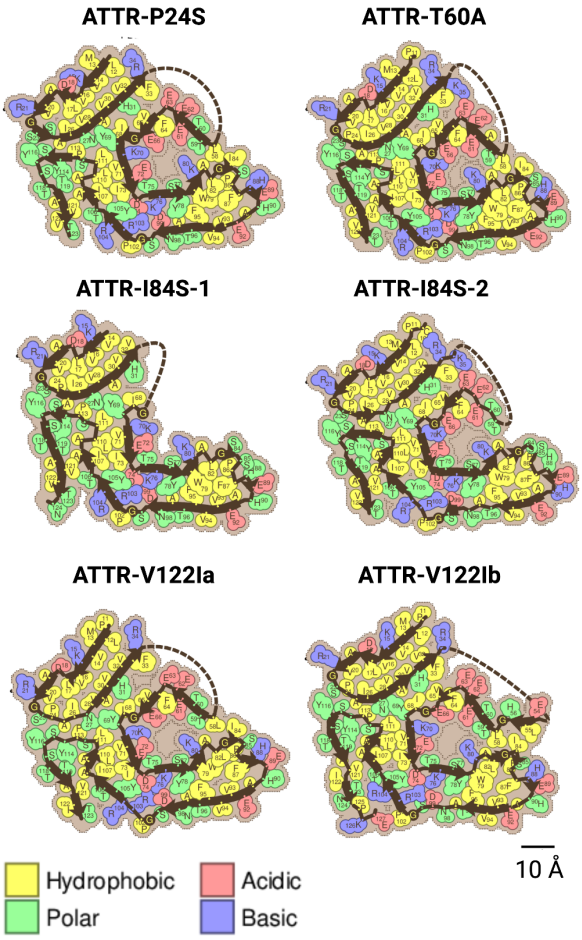

Supplementary Figure 5. Schematic view of ATTRv fibrils showing residue composition. Residues are color-coded by amino acid category, as labeled.

Supplementary Tables

Supplementary Table 1. List of ATTR samples included in the study.

Genotype	Origin	Sex	Age at collection	Neuropathy signs
ATTRwt-1	Autopsy	Male	78	No, but amyloid found at autopsy
ATTRwt-2	Transplant	Male	70	No
ATTRP24S	Transplant	Male	65	No
ATTRT60A	Autopsy	Male	57	Moderate
ATTRI84S-1	Autopsy	Female	56	No, but amyloid found at autopsy
ATTRI84S-2	Autopsy	Male	53	Mild
ATTRV122I	Autopsy	Male	Unknown	Unknown

Supplementary Table 2. Data collection and refinement statistics.

Data collection	wt-1	wt-2	P24S	T60A	I84S-1	I84S-2	V122I
Microscope	Titan Krios	Titan Krios	Titan Krios (G3i)	Titan Krios (G3i)	Titan Krios (G3i)	Titan Krios (G3i)	Titan Krios (G3i)
Acceleration Voltage (kV)	300	300	300	300	300	300	300
Detector	K3	K3	K3	K3	K3	K3	K3
Software	SerialEM 3.8	SerialEM 3.8	EPU	SerialEM 3.8	EPU	EPU	EPU
Magnification	165,000x	165,000x	81,000x	81,000x	81,000x	105,000x	105,000x
Pixel size at detector (Å/px)	0.53	0.53	1.1	0.53	1.1	0.86	0.86
Defocus range (μm)	-1.0 to -2.2	-1.0 to -2.2	-1.5 to -2.1	-1.4 to -2.2	-1.5 to -2.1	-0.8 to -2.1	-0.8 to -2.1
Total dose (e)	46	46	50	42	50	50	50
Exposure time (sec)	2.4	2.4	3	2.2	3	1.81	2.5
Number of movie frames	51	51	33	57	33	40	35
Reconstruction							
Usable micrograph	3295	2698	6981	3735	7223	9266	6479
Box size (pixel)	256	320	350	320	256	300	320
Total extracted segments	316273	113021	218699	121681	136825	233239	188814
Number of segments after 2D	151781	98223	169747	108550	90882	180431	142890* & 143138**
Number of segments after 3D	80229	34255	45958	43507	37130	98953	57804* & 61933**
Symmetry imposed	C1	C1	C1	C1	C1	C1	C1
Helical rise (Å)	4.75	4.78	4.84	4.79	4.75	4.758	4.76
Helical twist (°)	1.25	1.29	1.275	1.26	1.25	1.25	1.23* & 1.27**
Crossover length (Å)	684	663.3	670.6	677.5	684	682.9	695* & 673**
B factor	-79.23	-109.35	-142.98	-90.31	-91.2	-75.03	101.3* & 102.2**
Map resolution (Å; FSC=0.143)	3.31	3.7	3.65	3.3	3.61	3.07	3.16* & 3.2**
Map resolution (Å; FSC=0.5)	3.68	4.5	4.12	3.75	4.04	3.58	3.85* & 3.88**

Total number of straight filaments	3716	4693	48717	4201	2891	8237	26379
Total number of curvy filaments	126640	98223	169747	102844	90882	180431	142890
Straight fibril particles (%)	2.93	4.78	28.7	4.08	3.18	4.57	18.46